ACSNANO
www.acsnano.org
ARTICLE

# Electrochemically Programmable Plasmonic Antennas

Shi Dong,[†,§] Kai Zhang,[‡,§] Zhiping Yu,[†] and Jonathan A. Fan*[,‡]

[†]Institute of Microelectronics, Tsinghua University, Beijing 100084, China
[‡]Department of Electrical Engineering, Stanford University, Stanford, California 94305, United States

Supporting Information

**ABSTRACT:** Plasmonic antennas are building blocks in advanced nano-optical systems due to their ability to tailor optical response based on their geometry. We propose an electrochemical approach to program the optical properties of dipole antennas in a scalable, fast, and energy-efficient manner. These antennas comprise two arms, one serving as an anode and the other a cathode, separated by a solid electrolyte. As a voltage is applied between the antenna arms, a conductive filament either grows or dissolves within the electrolyte, modifying the antenna load. We probe the dynamics of stochastic filament formation and their effects on plasmonic mode programming using a combination of three-dimensional optical and electronic simulations. In particular, we identify device operation regimes in which the charge-transfer plasmon mode can be programmed to be "on" or "off." We also identify, unexpectedly, a strong correlation between DC filament resistance and charge-transfer plasmon mode frequency that is insensitive to the detailed filament morphology. We envision that the scalability of our electrochemical platform can generalize to large-area reconfigurable metamaterials and metasurfaces for on-chip and free-space applications.

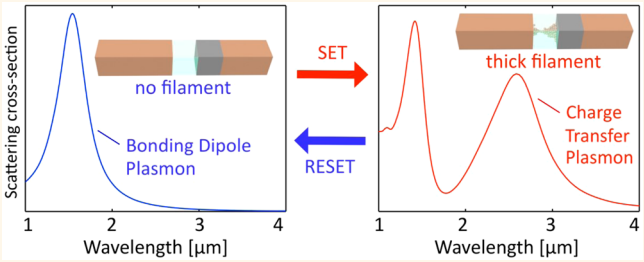


**KEYWORDS:** *plasmonics, antenna, programmable, kinetic Monte Carlo, FDTD, CBRAM*

Optical antennas are central elements in the next generation of miniaturized optical systems because their optical near- and far-field responses can be specified by their geometric layouts. This ability to engineer optical response by design stems from their support of surface plasmons, which are oscillations of free electrons in metal that are coupled with electromagnetic fields.[1] Arrays of antennas are the basis for metamaterials and metasurfaces, which are capable of supporting a wide range of magnitude and phase responses.[2] Plasmonic antennas also serve as sensors and probes in biological imaging and therapeutics platforms[3] and have been integrated with LEDs,[4] lasers,[5] fiber optics,[6] detectors,[7] modulators,[8] and solar cells[9] to improve baseline performance.

For the vast majority of plasmonic antenna technologies, optical responses are fixed once the antennas are fabricated. As such, a principal challenge in the field has been to identify ways to tune or program their optical response. Dynamically reconfigurable antennas would enable ultrabroadband sensors and detectors, infrared spatial light modulators, and dynamic switches and interferometers in on-chip photonic platforms. More generally, a programmable metasurface system would introduce versatility and flexibility to nano-optics hardware that would circumvent the need for a new device to be fabricated every time a new optical response is required.

Many antenna tuning strategies are based on modifying the dielectric environment near the antenna. One such approach utilizes carrier density changes in a semiconductor[10−12] or graphene[13] layer near the antenna by means of electronic charge injection, charge build-up at a Schottky barrier,[14] or optical generation of carriers.[15] In these approaches, the antenna load is modified because the Drude-like dielectric responses of these materials change with carrier concentration. While this approach is potentially very fast, its overall tuning bandwidth is limited. Another approach is to use materials, such as vanadium oxide[16] or germanium-antimony-tellurium,[17] which have refractive indices that change in response to electronic or thermal biasing. While effective, these tuning mechanisms have bandwidth and operating wavelengths that are limited by the physical properties of the specific materials. Other strategies employ liquid crystals,[18] nonlinear materials,[19] and MEMS devices,[20] which are difficult to scale down to the single antenna limit.

We propose an electrochemical approach to programming the response of individual dipole antennas in a scalable, fast, and energy efficient manner. The concept utilizes the antenna arms as electrodes in an electrochemical cell and is based on principles employed in conductive-bridge random access

Received: March 24, 2016
Accepted: June 21, 2016
Published: June 21, 2016

Downloaded via STANFORD UNIV on July 25, 2018 at 23:00:34 (UTC).
See https://pubs.acs.org/sharingguidelines for options on how to legitimately share published articles.

 © 2016 American Chemical Society 
DOI: 10.1021/acsnano.6b02031
ACS Nano 2016, 10, 6716−6724

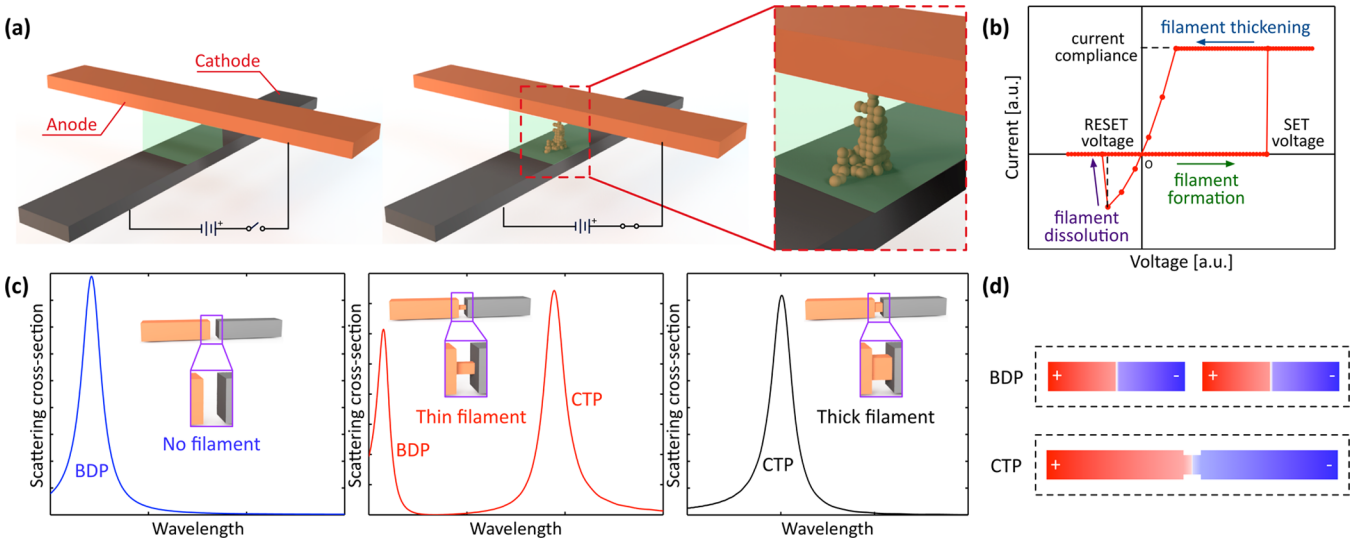


**Figure 1. Overview of programmable plasmonic antennas. (a) Schematic of stochastic filament growth in a CBRAM memory cell. (b) Typical current−voltage plot of a CBRAM cell, capturing filament growth and dissolution. (c) Scattering spectra of a dipole antenna loaded with no filament (left), a thin filament (middle), and a thick filament (right). (d) Surface charge distributions of the BDP and CTP modes.**

memory (CBRAM), which is an established form of nonvolatile electronic memory.[21−24] Individual CBRAM cells consist of two metallic wires separated by a solid electrolyte (Figure 1a). One of the wires comprises an electrochemically inert material and serves as the cathode, while the other wire comprises an electrochemically active material and serves as the anode. When a voltage is applied between the wires, metal from the anode migrates as ions into the electrolyte and reduces onto the cathode, forming a bridging metal filament. This process is reversible, as the filament dissolves upon application of a reverse bias. The growth and dissolution of the filament are reflected in the device current−voltage plot (Figure 1b).

In our antenna scheme, two antenna arms are separated by a solid electrolyte, forming a lateral CBRAM cell. As an electrical bias is applied between the antenna arms, a conductive filament grows within the electrolyte and bridges the two arms. The controllable growth of a bridging filament introduces a level of optical tuning control that enables not only fine shifts in mode frequency but also the creation of optical modes. These optical tuning regimes are described in Figure 1c. If there is no filament, the lowest order antenna mode is the capacitively coupled bonding dipole (BDP) mode, which supports a dipolar charge distribution in each antenna arm (Figure 1d). As a filamentary bridge forms, a charge transfer plasmon (CTP) mode emerges.[25−28] The CTP mode supports a dipolar charge configuration that is distributed throughout the entire bridged antenna (Figure 1d).

We can clearly see here that the growth and dissolution of a bridging filament can cause the CTP mode to modulate between the "on" and "off" states. In addition, further filament thickening leads to gradual and controllable blue-shifting of the CTP mode. As such, our device can be described as a plasmonic analogue to the memristor.[29] Our use of an electrochemical mechanism to tune optical nanostructures builds on prior studies that applied related mechanisms to tune plasmonic resonances[30,31] and modulate transmission in photonic waveguides.[32,33]

It is noted that there are other forms of electrochemical resistance switching memories, such as those based on oxygen anion transport in metal oxide materials.[34,35] While these electrochemical processes are effective at producing conductive filaments based on oxygen vacancies at DC frequencies, they do not apply to our system because such filaments do not possess high conductivity at infrared frequencies. Our scheme requires metallic filaments, which yield a large negative permittivity at these frequencies.

Is it feasible to use electronic filament growth to control the response of optical antennas? A qualitative comparison of CBRAM cells with plasmonic antennas suggests synergy at multiple levels. First, many metals used in CBRAM, such as silver and copper, are excellent optical materials with relatively low optical absorption losses. Second, CBRAM cells can be scaled down to devices with footprints in the hundreds of square nanometers range, which matches the length scales associated with plasmonic antennas. Third, the filaments generated in CBRAM can be grown to possess nanoscale diameters, producing low resistances. We also note that CBRAM has been developed to the point of commercialization,[36] indicating that the electrochemical control of filaments is a robust and reliable mechanism in electronic programming. In fact, the proven scaling of CBRAM to systems containing millions of memory cells suggests the generalization of our platform to macroscale arrays of independently addressable antennas. Such a technology platform can serve as programmable infrared and terahertz metamaterials and metasurfaces for on-chip and free-space applications.

To investigate our hybrid plasmonic-electronic antenna system, we use a combination of optical and electronic simulation tools to quantify the relationship between electrochemical filament growth and antenna optical response. We characterize optical response using the finite-difference time-domain (FDTD) method, which is an established tool in nanoplasmonics modeling.[37] We simulate the electrochemical filament growth and dissolution process using three-dimensional kinetic Monte Carlo (3D KMC) simulations. Similar to other filament growth models,[38] KMC models can yield electronic parameters that agree well with experimental data (Figure S4). Additionally, the KMC method can capture the detailed morphology of the filaments.[39] Our coupled FDTD and KMC simulation approach allows us to study the direct


DOI: 10.1021/acsnano.6b02031
ACS Nano 2016, 10, 6716−6724

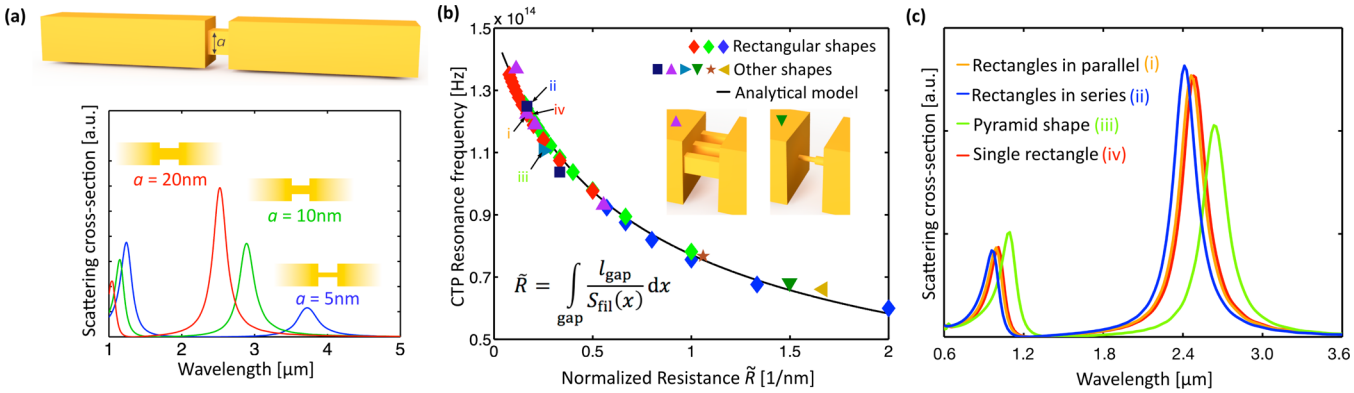


**Figure 2. Gold dipole antennas loaded with simple filament geometries. (a) Spectra of gold dipole antennas loaded with rectangular metal filaments of differing cross-sectional dimension. *a* is the filament width. (b) Plot of CTP mode resonance frequency as a function of normalized resistance for nine different type of filament shapes. The geometry of two such filaments is shown in the inset, along with the expression for normalized filament resistance. $l_{gap}$ is the width of the antenna gap, and $S_{fil}(x)$ is the filament cross-sectional area as a function of position *x* in the gap. (c) Spectra of four dipole antennas loaded with filaments possessing similar electrical resistances but differing shapes. The CTP resonance frequencies of these antennas are marked in (b).**

impact of stochastic filament growth on antenna optical response in three dimensions.

## RESULTS AND DISCUSSION

We begin with an analysis of dipole antennas loaded with well-defined nonstochastic filaments. This study is required before the more complex behavior of stochastic filament systems can be interpreted. The loading of dipole antennas with conductive filaments has been a topic of intensive study. In early seminal work, antennas with simple bridging filament geometries were characterized. These filaments consisted of pure metal, and the filaments and antenna gaps were modeled using classical antenna theory as parallel impedance elements.[28] For wide filaments, the antenna load impedances were inductive and the antenna supported the CTP mode. For filaments below a critical width, the antenna load impedances were capacitive and the antenna supported the BDP mode. There has also been extensive work on dipole antenna loading in the context of quantum plasmonic tunneling,[25,26] where the correlation between the CTP mode frequency and gap conductivity was quantified.

We will focus our study here on the relationship between filament DC electrical resistance and the CTP mode resonance for filaments of different shapes. DC electrical resistance is a central parameter in our electrochemical system because it can be measured and controlled during the filament growth process. For this analysis, we will simulate all-gold dipole antennas and filaments, which do not represent electrochemical systems but are nonetheless suitable for our study of antenna loading. By analyzing antennas with symmetric antenna arms and constant material composition, the optical modes can be readily quantified without artifacts arising from material or geometric asymmetry.

For filaments possessing a square cross-section, the relationship between filament resistance and CTP mode line shape is visualized in Figure 2a. The gold antenna possesses a 20 nm gap ($l_{gap}$) and arms 300 nm long ($l_{arm}$), 40 nm wide ($w_{arm}$), and 40 nm thick ($t_{arm}$). The filament and antenna cross sections are axially aligned. For a filament with high resistance (*i.e.*, small physical cross-section), the CTP mode is clearly visible and is strongly red-shifted relative to the BDP mode, with a resonant wavelength near 4 $\mu$m. As the filament resistance decreases (*i.e.*, filament cross-section increases), the CTP mode blue-shifts and increases in magnitude, converging toward the CTP mode of an ideal single-rod nanoantenna. The correlation between CTP mode resonant frequency and normalized filament resistance ($\tilde{R}$), which is defined as the filament resistance (R) divided by the resistivity of gold ($\rho$) and has units nm$^{-1}$, is plotted in Figure 2b. To convert $\tilde{R}$ to resistance (*i.e.*, units of ohms) for gold, it can be multiplied by 24.

What happens to this correlation as the filament deviates from a square cross section? Filament inductance and gap capacitance determine the electric and magnetic field distribution within and around the gap and are therefore sensitive to the three-dimensional filament and gap geometry. We simulate antennas loaded with a broad range of filament geometries and calculate the lineshapes and spectral positions of the corresponding CTP modes. The filament layouts are described in detail in the Supporting Information and include linear rods with a range of cross sections, truncated pyramids, truncated cones, stacks of rods, simple branches, and multiple linear rods (Figure S6). We define linear structures as those with straight and constant cross sections over their entire lengths. The resistances of these filaments can be calculated with exact analytic expressions.

The results are plotted in Figure 2b and show that the correlation between CTP frequency and DC filament resistance is strong and is relatively insensitive to the exact filament shape. As such, DC resistance measurements are sufficient to determine and specify the CTP resonance wavelength in these systems. This result is significant in evaluating the feasibility of our tuning mechanism: with electrochemical filament growth, the filament resistance can be monitored and specified but its shape and location within the gap cannot be controlled. The full scattering spectra from antennas possessing filaments with similar resistance but different geometries are displayed in Figure 2c. These plots show that the CTP mode peak positions, magnitudes, and lineshapes are consistent for all antennas.

To further understand the trends in this correlation, we examine our antennas in the context of a lumped circuit model.[40−44] The gap load and antenna arms each are modeled as impedance elements, and together, they form a closed parallel circuit (Figure 3a). The antenna arms are modeled as


DOI: 10.1021/acsnano.6b02031
ACS Nano 2016, 10, 6716−6724

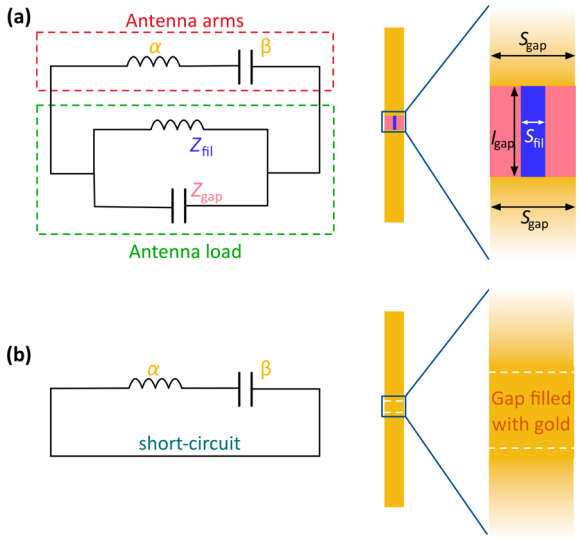


**Figure 3. Antenna nanocircuit model. (a) A filament-loaded dipole antenna can be modeled as a lumped circuit, where the antenna arm and filament load are parallel impedance elements. (b) A dipole antenna loaded completely with metal can be treated as a single-rod nanoantenna and modeled as a short-circuited antenna arm impedance element.**

series LC elements and possess an inductance $\alpha$ and capacitance $\beta$. The antenna load comprises an inductive filament and a capacitive gap in parallel. In this model, we neglect resistive elements representing radiative and ohmic loss channels. Our focus here is on the dependence of antenna resonance frequency on filament geometry, which is a function only of inductance and capacitance.

In the limit where the antenna gap is filled with gold, the antenna resembles an ideal single-rod nanoantenna and supports a well-defined CTP mode in the thick-filament regime (Figure 3b). The antenna load can be described as a short circuit, and the entire antenna circuit forms an LC tank with a resonant angular frequency $\omega_0 = 1/\sqrt{\alpha\beta}$ (Figure 3b). For a gold antenna in air with dimensions defined above, $\omega_0$ is simulated to be $9.4 \times 10^{14}$ Hz. The impedance load contribution from the antenna arms $Z_{arm}$ at any frequency $\omega$ can now be expressed as

$$Z_{arm} = i\left(\omega\alpha - \frac{1}{\omega\beta}\right) = i\omega\alpha\left(1 - \frac{\omega_0^2}{\omega^2}\right) \tag{1}$$

Our antenna loads with thin filaments can also be expressed explicitly. The impedance of a linear gold filament possessing a constant physical cross-section $S_{fil}$ is $Z_{fil} = -\frac{i}{\varepsilon(\omega)}\frac{l_{gap}}{S_{fil}}$, where $\varepsilon(\omega)$ is the dielectric constant of gold. For negative $\varepsilon(\omega)$, this impedance element has a positive imaginary contribution and is inductive. The impedance of the gap is $Z_{gap} = -\frac{i}{\varepsilon_b}\frac{l_{gap}}{(S_{gap} - S_{fil})}$, where $\varepsilon_b$ is the gap dielectric and $S_{gap} = w_{arm}t_{arm}$ is the physical cross-section of the gap. This impedance element has a negative imaginary contribution and is capacitive.

The total antenna system is resonant when $\mathrm{Im}(Z_{arm} + Z_{gap} \parallel Z_{fil}) = 0$. This expression can be written in terms of normalized filament resistance, where $\tilde{R} = l_{gap}/S_{fil}$ is exact for resistors of constant cross section. The condition for CTP mode resonance in terms of $\tilde{R}$ is

$$\varepsilon_0\omega\alpha\left(1 - \frac{\omega_0^2}{\omega^2}\right) \times \mathrm{Re}\left(\left(\varepsilon_b - 1 - \frac{\omega_p^2}{\omega(\omega + i\gamma)}\right)\tilde{R} + \omega\frac{1}{\frac{S_{gap}}{l_{gap}} - \tilde{R}}\right) = 1 \tag{2}$$

The solution from this analytic model is plotted as a black line in Figure 2b, where a single fitting parameter $\alpha$ is used. This model agrees well with the numerically obtained data points.

For linear filaments with the same DC resistance, the independence of CTP mode frequency with respect to filament cross-section shape is directly captured in the analytic model. Here, the CTP mode frequency depends only on the filament cross-sectional area $S_{fil}$ and is the same irrespective of whether the filament is rectangular or circular, or whether the antenna load consists of multiple filaments with a total cross sectional area $S_{fil}$. It also is independent of filament position within the antenna gap. This observation is consistent with the physical description of the gap as a parallel plate capacitor, where electric field lines run in parallel from one plate to the other.

For nonlinear filament geometries such as cones, we can use a series of approximations to recover the relationship between CTP mode frequency and $\tilde{R}$ specified in eq 2. Starting with filament impedance, we approximate the filament load as a sum of cross-sectional contributions over the total filament length: $Z_{fil} \approx -\frac{i}{\varepsilon(\omega)}\int_0^{l_{gap}}\frac{l_{gap}}{S_{fil}(x)}\,dx$. The integrand can be approximated as the normalized resistance, so that $Z_{fil} \approx -\frac{i}{\varepsilon(\omega)}\tilde{R}$ and the filament impedance term in eq 2 is recovered. A similar approach can recover the gap impedance term in eq 2. This impedance approximation assumes that each cross-sectional segment of our filament is equipotential under electric field bias, and it is valid for axially symmetric filament loads that possess uniform cross sections along their length. For irregularly shaped filaments, this assumption breaks down, but the error produced from our approximation method is modest for filaments with cross sections that do not strongly vary with length. For the DC resistance of conelike shapes with modest vertex angles, the error produced from our approximation, as compared to the exact solution, is within 10%.[45]

For the next part of our analysis, we consider the growth and dissolution of stochastic filament geometries in electrochemical dipole antenna systems. Our first task is to select the anode, cathode, and solid electrolyte materials in our system. For antennas, we require electrode materials that possess sufficiently low optical loss and an electrolyte that can support the growth of sufficiently large and continuous filaments. We specify the anode antenna arm to be copper, the cathode antenna arm to be copper with a platinum plug, and the solid electrolyte to be copper sulfide. Copper is an excellent plasmonic material,[46,47] and while platinum is not a traditional plasmonic material, it possesses acceptable losses at infrared wavelengths.[48] Copper sulfide is a proven solid electrolyte material[49,50] that has been demonstrated to (1) scale down to devices with active areas in the tens of square nanometers range and (2) support continuous and large filaments with low resistances. In this analysis, we will focus on filament loading in geometrically symmetric dipole antennas and disregard substrate or electronic lead contributions. The latter can be


DOI: 10.1021/acsnano.6b02031
ACS Nano 2016, 10, 6716−6724

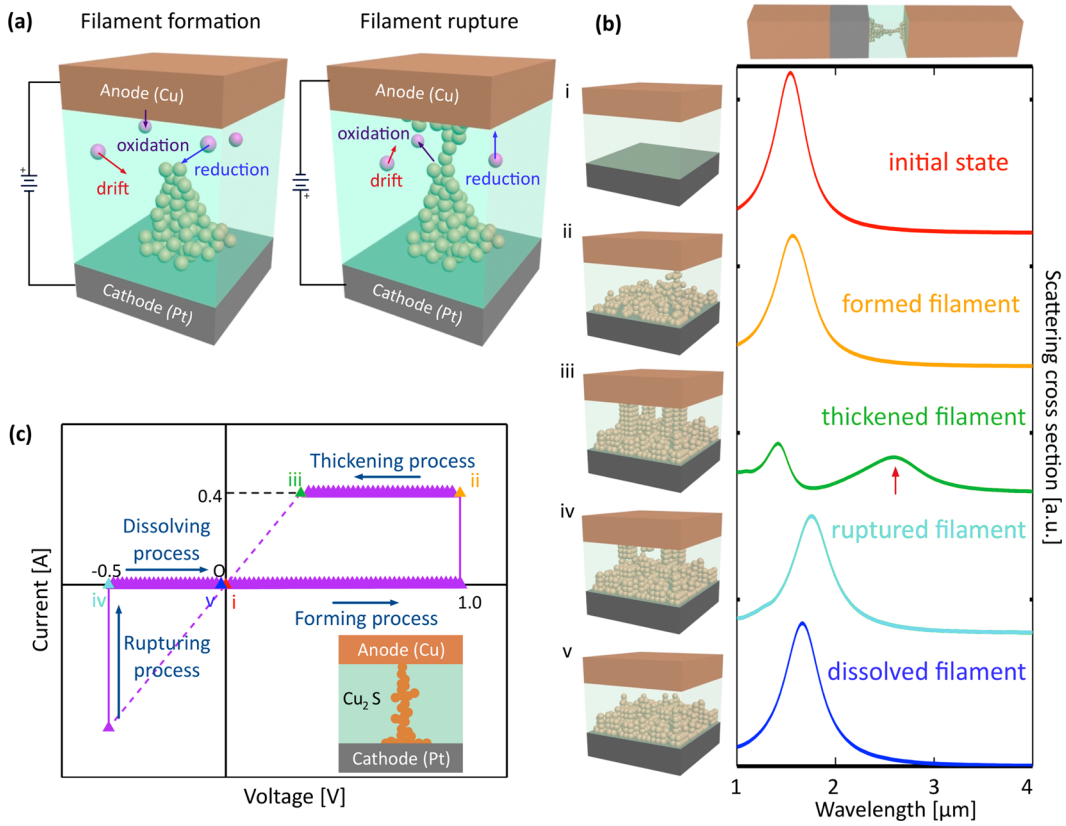


**Figure 4. Summary of dipole antenna loading with stochastic filaments. (a) Schematic of the copper reduction, oxidation, and ion-drift processes accounted for during filament forming and dissolution in the KMC model. (b) Scattering spectra and (c) corresponding current−voltage plot of a platinum−copper dipole antenna loaded with a stochastic copper filament at different stages of filament growth and dissolution.**

introduced without substantially perturbing the antenna modes by judicious placement of metal leads to the antenna arms[51] or by using transparent lead materials.[52,53]

The stochastic dynamics of filament growth and dissolution are modeled with three-dimensional KMC simulations. In this method, the CBRAM cell is discretized into a fine grid, and the CBRAM switching process is captured in discrete time intervals. Within each time interval, one of the following processes can occur with a certain probability (Figure 4a): (1) a metal atom cluster on the anode surface is oxidized into an ion cluster and enters the electrolyte layer, (2) an ion cluster within the electrolyte moves from one grid to an adjacent grid, and (3) an ion cluster is reduced on the surface of the cathode or the filament, becoming part of the filament itself. These probabilities are governed by the filament temperature and energy barriers associated with atomic-scale oxidation, diffusion, and reduction. The simulation parameters are in the Supporting Information.

The scattering spectra of an antenna at differing stages of filament growth and dissolution are plotted in Figure 4b, together with their associated filament geometries. The dipole antennas have the same geometric parameters as the gold antennas above. The dielectric constants of copper, platinum, and copper sulfide are taken from standard literature sources,[47,48,54] and the energy barrier parameters for KMC are extracted from experimental results.[55] Five states of filament growth and dissolution are captured: (i) the initial state with no filament load, (ii) the state at which the filament just forms a conductive bridge, (iii) the state at which the filament is thickest, (iv) a state representing filament dissolution, to the point of rupture, and (v) a state representing nearly complete filament dissolution. The IV curve of the filament growth and dissolution process is plotted in Figure 4c, together with points demarking these five states.

These spectra show that the initial state, which possesses no filament load, supports a clear BDP mode with a resonance near 2 $\mu$m. This result indicates that our heterometallic antenna, consisting of unconventional plasmonic materials, can support a clear plasmonic dipole mode. As the filament initially grows (ii), the resistance between the two antenna arms decreases, as signified by the jump in the IV curve. However, the spectrum exhibits minimal change because the filament is extremely thin and does not yet significantly contribute to the total antenna load. As the filament grows to sufficient thickness (iii), the CTP mode emerges (red arrow). As such, electrochemical filament growth can turn the CTP mode "on" and "off". As the filament partially dissolves (iv), its conductivity decreases, which red-shifts and ultimately turns "off" the CTP mode. Finally, the BDP mode blue-shifts towards its initial peak wavelength in (i) as the filament further dissolves (v).

The CTP mode resonance frequency is a strong function of stochastic filament resistance. To probe this relationship, we simulate all-copper dipole antennas loaded with stochastic copper filaments of different morphologies and resistances. Even though all-copper antennas do not correspond to a physical electrochemical system, we simulate them here because they possess a clearly defined CTP mode frequency that can be processed in our analytic model. A plot of CTP mode


DOI: 10.1021/acsnano.6b02031
ACS Nano 2016, 10, 6716−6724

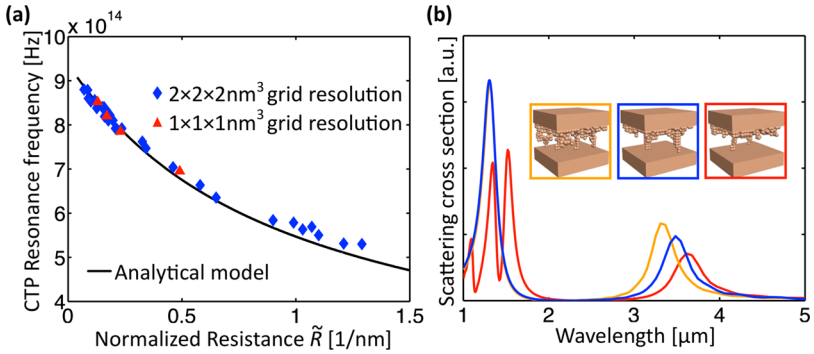


**Figure 5. Copper dipole antennas loaded with stochastic filaments. (a) Plot of CTP mode frequency *vs* normalized filament resistance for copper antennas loaded with stochastic copper filaments. (b) Scattering spectra of three different antennas, each loaded with a filament of $\tilde{R}$ = 1.29 (red), 1.03 (blue), and 0.90 (orange). The inset shows images of each stochastic filament geometry.**

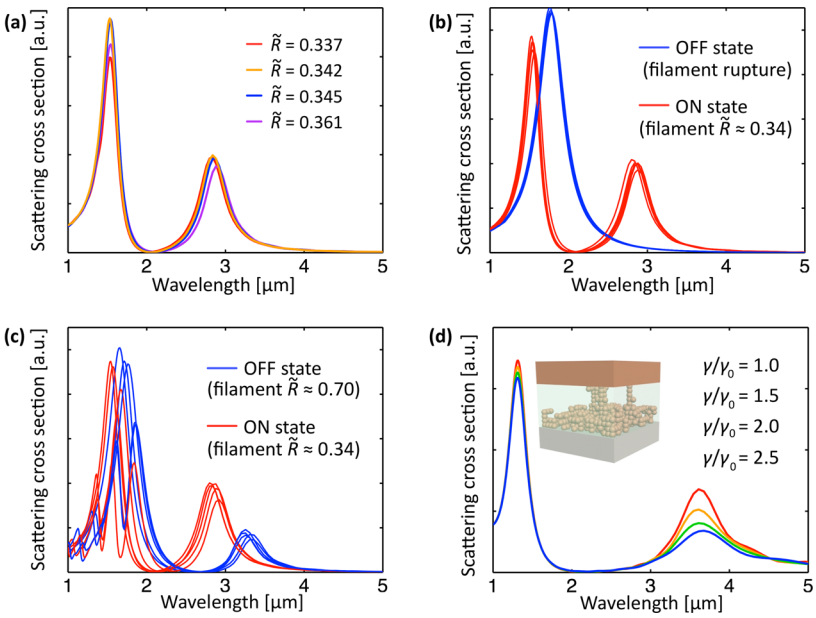


**Figure 6. Copper−platinum antennas loaded with stochastic filaments. (a) Spectra of four dipole antennas, each loaded with copper filaments of similar electrical resistance but differing morphology. (b) Spectra of a dipole antenna that has been cycled between an ON state ($\tilde{R} \sim 0.34$) and OFF state (filament is completely dissolved). (c) Spectra of a dipole antenna that has been cycled between an ON state ($\tilde{R} \sim 0.34$) and OFF state ($\tilde{R} \sim 0.70$). (d) Spectra of a dipole antenna loaded with a copper filament of constant DC resistance but differing Drude loss coefficient.**

frequency *vs* normalized filament resistance is displayed in Figure 5a for 25 different antennas and demonstrates a clear correlation. The electrical resistance for each stochastic filament shape is calculated using a resistor network approach, which is described in the Supporting Information. To convert $\tilde{R}$ to resistance (*i.e.*, units of ohms) for copper, it can be multiplied by 17. Interestingly and importantly, these simulated data points fit well with our analytic model relating CTP mode frequency with normalized resistance (Figure 5a, black line). This result indicates that optical antenna loading is not very sensitive to the atomic-scale filament morphology.

The insensitivity of the CTP mode resonance to detailed filament geometry enables precise CTP mode tuning based on electrical resistance measurements. As a demonstration, we simulate the optical properties of four all-copper antennas, each loaded with stochastic filaments of different resistance (Figure 5b). As the resistances of the filaments decrease, the CTP mode frequency blue-shifts, in agreement with our analytic model. For all three spectra, the peak CTP mode frequency is within 6% of that calculated from our analytic model, in spite of the fact that the filament morphologies are stochastic (Figure 5b, inset). The variation in BDP mode lineshapes for these different antennas appears to be mediated by asymmetries in the filaments and will be the subject of future study.

We now focus on simulations of copper−platinum dipole antennas loaded with stochastic filaments and copper sulfide electrolyte, which represent our programmable antenna system. To further gauge the relationship between spectra and filament resistance, we calculate the scattering spectra of antennas loaded with filaments of similar resistance but differing morphology. The results are plotted in Figure 6a for four antennas, each with $\tilde{R}$ between 0.33 and 0.37. These spectra show that the CTP mode magnitudes and line widths are consistent, with peak resonant wavelengths near 2.8 $\mu$m.

A major feature of electronically programmable systems is their ability to cycle. As such, we simulate and characterize the cycling of our dipole antennas in two regimes. In the first, the CTP mode is cycled between an "on" state, which is


DOI: 10.1021/acsnano.6b02031
ACS Nano 2016, 10, 6716−6724

represented by growth of a thick filament, and an "off" state, which is represented by full filament rupture. This regime represents the full dynamic range of CTP mode modulation and is suitable in broadband applications that require a mode to completely turn "on" and "off." Simulated scattering spectra of a dipole antenna over the course of five full cycles indicate that the CTP mode can be turned "on" and "off" with high fidelity over the course of many switching events (Figure 6b). The spectra demonstrate the robustness of the CTP mode frequency to morphological variations during cycling and is consistent with the result in Figure 6a. In comparing the position of the BDP mode of the antenna in the "initial" state, which has no metal in the antenna gap, with that of the antenna in the "off" state, discrepancies arise because the remnants of the filament in the "off" state still partially load the antenna.

In the second cycling regime, the filament is cycled between a high and low resistance state, such that the CTP mode merely shifts instead of disappears. Here, the magnitude of the low resistance CTP mode at its peak frequency modulates from high to nearly zero. As the spectra in Figure 6c indicate, the CTP modes in both states retain their peak position and magnitude over cycling. Compared to the cycling regime with complete filament rupture, this regime of partial filament dissolution requires less transport of copper atoms and ions within the antenna gap and therefore enables higher-speed operation and greater mode-switching durability. The advantage in operation speed can be extracted directly from the KMC simulations, which reveal that switching times that are approximately 25% faster compared to that involving complete filament rupture. It is noted that these cycling simulations do not incorporate irreversible metal ion transport pathways, which set general limits to cycling robustness in CBRAM devices. These simulations nonetheless suggest the potential for predictable and reliable plasmonic mode programming.

All of the simulations to this point assume that the dielectric constant of the copper filament is that of bulk copper. Realistically, the quality of the filamentary metal will not be that of bulk metal but that of a more lossy material. Losses in our system arise from multiple sources, including contact resistance losses between copper and platinum, ionic impurities within the copper, and quantum effects due to enhanced electron-surface collisions in our size-reduced system. To understand how losses impact our CTP mode, we calculate the spectra of antennas loaded with copper filaments of constant morphology but different Drude loss coefficient. The spectra (Figure 6d) show that the CTP mode decreases in magnitude as losses increase, as expected. Nonetheless, even with a 2.5 times increase in Drude loss, the CTP mode is still clearly visible and well-defined.

The copper/copper sulfide/platinum material system studied here is just one materials combination that can be used in our programmable optics platform. In addition, there exist alternative antenna geometries beyond the dipole antenna that can expand the scope of programmable optical responses. These include antennas with multiple arms and nonlinear geometries.[56−59] A more detailed discussion of alternative antenna materials and geometries is provided in the Supporting Information.

## CONCLUSION

Electronic systems are remarkably versatile technologies in part because they can be programmed to perform a diverse set of functions. In this study, we propose reconfigurable plasmonic antennas as an optical analogue to programmable electronic hardware. The electrochemical filament growth and dissolution programming mechanism is inspired by CBRAM electronics, and it can be used to turn plasmonic modes "on" and "off" in nonvolatile ways. Our analysis of dipole antennas loaded with both simple and stochastic filament geometries reveals a strong relationship between resonant mode frequency and filament resistance, and we propose an analytic model that matches well with numerical simulation results. These concepts in programmable nano-optics can generalize to complex antenna layouts with multiple electrochemical cells, enabling a multitude of antenna configurations with a broad range of magnitude and phase responses. We envision that the scalability of these programmable electrochemical junctions will enable programmable metamaterials and metasurfaces that operate at infrared and terahertz frequencies.

## METHODS

**Kinetic Monte Carlo Simulations.** We perform 3D KMC simulations using custom Matlab coding scripts. Filament dynamics can be broken down into four processes: forming, thickening, rupturing, and dissolution. The dynamics of each process is captured through a series of time steps, where stochastic ion motions and redox processes are calculated in a quasistatic way during each time step. Specific simulation parameters are listed in the Supporting Information.

The forming process is simulated in a regime of constant voltage. At the beginning of each time step, the electrostatic potential distribution within the solid electrolyte is obtained by solving Poisson's equation in 3D within the entire simulation volume. It is assumed that the filament and electrodes are equipotentials with known values, and periodic electric potential conditions are set at the lateral boundaries of the cell. Next, the probabilities for copper to undergo a state change (*i.e.*, oxidation, reduction, or drift) is calculated for every ion and atom of copper in the simulation window. The probabilities are computed from the potential distribution and the corresponding energy barriers, and the parameters used for these calculations are listed in Table S1. Finally, on the basis of the probabilities, a single redox or drift process is randomly selected to take place for a single copper ion or atom. The process then iterates to the next time step and repeats.

The thickening process begins when the filament shunts the anode and cathode. In our simulations, the temperature in the filament only increases by approximately 10 °C during this process, so we neglect heating effects. We perform these simulations at the compliance current $I_C$. This constant current simulation regime requires us to calculate the resistance of the filament at each time step, which determines the applied electrode voltage $V = I_C R$. To calculate total filament resistance, we use a resistor network model that discretizes the filament into a network of tiny resistors (Figure S1). By applying Kirchhoff's current law to this network, we can calculate the total filament resistance and potential difference between the electrodes.

With these parameters, the electric potential boundary conditions are specified and the potential distribution within the switching layer is obtained by solving Poisson's equation. The ionic redox and drift processes are modeled in the same way as those in the forming process. As the filament thickens over multiple time steps, the potential difference between the electrodes decreases with the filament resistance. The vertical electric field across the switching layer weakens, reducing the oxidation rates at the anode surface. When no oxidation events occur within 1000 consecutive time steps, the filament thickening process is defined as complete.

The rupture process starts when a negative voltage bias is applied across the electrodes, causing current to flow through the filament. This process introduces significant Joule heating into the filament. To account for heating in our KMC model at each time step, we calculate the precise current flow through each branch of the filament using the resistor network and the Kirchoff's current law law. To calculate the temperature distribution within the antenna gap as a function of


DOI: 10.1021/acsnano.6b02031
ACS Nano 2016, 10, 6716−6724

current distribution, we use the thermal-electric equation, which is the Joule heating equation coupled with Fourier's law of thermal conduction.[60] With these temperature distributions, we adjust the redox and drift rates in our model,[39] which generally increase with an increase in temperature.

The rupture process transitions to the dissolution process when the device has ruptured to a point of high resistance. To characterize the start of this state, we calculate the tunneling current between the ruptured filament and anode at each time step using the Fowler-Nordheim equation.[61] We define the start of the dissolution process as the time when the tunneling current is negligible. The ion kinetics of this process is the exact opposite of those in the forming process, and copper atoms are oxidized from the filament residue and reduced at the anode electrode surface.

The nanoscale grid in our KMC model, which sets the spatial granularity of the filaments, is $2 \times 2 \times 2$ nm$^3$. Ideally, our KMC simulations would be discretized down to the atomic scale to track the dynamics of individual atoms. Copper atoms have a diameter of approximately four angstroms, setting the physical lower bounds of the simulation grid. For simulation windows spanning tens of thousands of cubic nanometers, this level of granularity is not computationally tractable. To test the validity of our coarse nanoscale grid approximation, we performed simulations that utilize smaller $1 \times 1 \times 1$ nm$^3$ grids. The simulations utilizing $2 \times 2 \times 2$ nm$^3$ grids converge with these simulations (Figure 5a), indicating that $2 \times 2 \times 2$ nm$^3$ grid resolution is sufficient for our application.

**Finite-Different Time-Domain Simulations.** We perform FDTD simulations using the commercial program Lumerical. The overall simulation setup includes two metal antenna arms loaded with a gap dielectric (*i.e.*, $Cu_2S$ electrolyte) and metal filament. The device as defined in the software, is visualized in Figure S5. The stochastic filament geometries are directly imported from our KMC simulation program. The dielectric constants of copper are modeled in the near- and mid-infrared with the Drude model $\varepsilon(\omega) = \varepsilon_\infty - \frac{\omega_p^2}{\omega(\omega + i\gamma)}$, where $\varepsilon_\infty$ is the high frequency permittivity, $\omega_p$ is the plasma frequency, and $\gamma$ is the damping coefficient.

Within the antenna gap, a mesh with $1 \times 1 \times 1$ nm$^3$ resolution ensures that the filament, which comprises $2 \times 2 \times 2$ nm$^3$ voxels, has a sufficiently fine mesh. The boundaries of the mesh are specified to match with the boundaries of the filament voxels (Figure S5b). Perfectly matched layers at the edges of the FDTD simulation window minimize nonphysical reflection effects in the simulation. The total-field scattered-field methodology is combined with frequency domain power monitors to measure the total scattering cross sections of the nanostructures.

## ASSOCIATED CONTENT

### Supporting Information

The Supporting Information is available free of charge on the ACS Publications website at DOI: 10.1021/acsnano.6b02031.

Additional experimental procedures and results (PDF)

## AUTHOR INFORMATION


### Corresponding Author

*E-mail: jonfan@stanford.edu.


### Author Contributions

[§]S.D. and K.Z. contributed equally.

### Notes

The authors declare no competing financial interest.

## ACKNOWLEDGMENTS

This work was supported by the U.S. Air Force under Award No. FA9550-15-1-0161. We acknowledge H. S. Philip Wong and B. Magyari-Kope for useful discussions, Y. Wang for help with the figures, and S. Doshay and K. Kanada for editorial assistance.

## REFERENCES


(1) Barnes, W. L.; Dereux, A.; Ebbesen, T. W. Surface Plasmon Subwavelength Optics. *Nature* **2003**, *424*, 824−830.

(2) Yu, N.; Capasso, F. Flat Optics with Designer Metasurfaces. *Nat. Mater.* **2014**, *13*, 139−150.

(3) Anker, J. N.; Hall, W. P.; Lyandres, O.; Shah, N. C.; Zhao, J.; Van Duyne, R. P. Biosensing with Plasmonic Nanosensors. *Nat. Mater.* **2008**, *7*, 442−453.

(4) Lozano, G.; Louwers, D. J.; Rodriguez, S. R. K.; Murai, S.; Jansen, O. T. A.; Verschuuren, M. A.; Gomez Rivas, J. Plasmonics for Solid-State Lighting: Enhanced Excitation and Directional Emission of Highly Efficient Light Sources. *Light: Sci. Appl.* **2013**, *2*, e66.

(5) Yu, N.; Fan, J.; Wang, Q. J.; Pflugl, C.; Diehl, L.; Edamura, T.; Yamanishi, M.; Kan, H.; Capasso, F. Small-Divergence Semiconductor Lasers by Plasmonic Collimation. *Nat. Photonics* **2008**, *2*, 564−570.

(6) Smythe, E. J.; Dickey, M. D.; Bao, J.; Whitesides, G. M.; Capasso, F. Optical Antenna Arrays on a Fiber Facet for in Situ Surface-Enhanced Raman Scattering Detection. *Nano Lett.* **2009**, *9*, 1132−1138.

(7) Fan, P.; Huang, K. C. Y.; Cao, L.; Brongersma, M. L. Redesigning Photodetector Electrodes as an Optical Antenna. *Nano Lett.* **2013**, *13*, 392−396.

(8) Cai, W.; White, J. S.; Brongersma, M. L. Compact, High-Speed and Power-Efficient Electrooptic Plasmonic Modulators. *Nano Lett.* **2009**, *9*, 4403−4411.

(9) Atwater, H. A.; Polman, A. Plasmonics for Improved Photovoltaic Devices. *Nat. Mater.* **2010**, *9*, 205−213.

(10) Dionne, J. A.; Diest, K.; Sweatlock, L. A.; Atwater, H. A. PlasMOStor: A Metal−Oxide−Si Field Effect Plasmonic Modulator. *Nano Lett.* **2009**, *9*, 897−902.

(11) Chen, H.-T.; Padilla, W. J.; Zide, J. M. O.; Gossard, A. C.; Taylor, A. J.; Averitt, R. D. Active terahertz metamaterial devices. *Nature* **2006**, *444*, 597−600.

(12) Chen, H.-T.; O'Hara, J. F.; Azad, A. K.; Taylor, A. J.; Averitt, R. D.; Shrekenhamer, D. B.; Padilla, W. J. Experimental Demonstration of Frequency-Agile Terahertz Metamaterials. *Nat. Photonics* **2008**, *2*, 295−298.

(13) Yao, Y.; Kats, M. A.; Shankar, R.; Song, Y.; Kong, J.; Loncar, M.; Capasso, F. Wide Wavelength Tuning of Optical Antennas on Graphene with Nanosecond Response Time. *Nano Lett.* **2014**, *14*, 214−219.

(14) Feigenbaum, E.; Diest, K.; Atwater, H. A. Unity-Order Index Change in Transparent Conducting Oxides at Visible Frequencies. *Nano Lett.* **2010**, *10*, 2111−2116.

(15) MacDonald, K. F.; Samson, Z. L.; Stockman, M. I.; Zheludev, N. I. Ultrafast Active Plasmonics. *Nat. Photonics* **2009**, *3*, 55−58.

(16) Kats, M. A.; Blanchard, R.; Genevet, P.; Yang, Z.; Qazilbash, M. M.; Basov, D. N.; Ramanathan, S.; Capasso, F. Thermal Tuning of Mid-Infrared Plasmonic Antenna Arrays Using a Phase Change Material. *Opt. Lett.* **2013**, *38*, 368−370.

(17) Michel, A.-K. U.; Chigrin, D. N.; Maß, T. W. W.; Schönauer, K.; Salinga, M.; Wuttig, M.; Taubner, T. Using Low-Loss Phase-Change Materials for Mid-Infrared Antenna Resonance Tuning. *Nano Lett.* **2013**, *13*, 3470−3475.

(18) Hsiao, V. K. S.; Zheng, Y. B.; Juluri, B. K.; Huang, T. J. Light-Driven Plasmonic Switches Based on Au Nanodisk Arrays and Photoresponsive Liquid Crystals. *Adv. Mater.* **2008**, *20*, 3528−3532.

(19) Kauranen, M.; Zayats, A. V. Nonlinear Plasmonics. *Nat. Photonics* **2012**, *6*, 737−748.

(20) Ou, J.-Y.; Plum, E.; Zhang, J.; Zheludev, N. I. An Electromechanically Reconfigurable Plasmonic Metamaterial Operating in the Near-Infrared. *Nat. Nanotechnol.* **2013**, *8*, 252−255.

(21) Valov, I.; Waser, R.; Jameson, J. R.; Kozicki, M. N. Electrochemical Metallization Memories—Fundamentals, Applications, Prospects. *Nanotechnology* **2011**, *22*, 254003.




DOI: 10.1021/acsnano.6b02031
*ACS Nano* 2016, 10, 6716−6724

(22) Celano, U.; Goux, L.; Belmonte, A.; Opsomer, K.; Franquet, A.; Schulze, A.; Detavernier, C.; Richard, O.; Bender, H.; Jurczak, M.; et al. Three-Dimensional Observation of the Conductive Filament in Nanoscaled Resistive Memory Devices. *Nano Lett.* **2014**, *14*, 2401−2406.
(23) Terabe, K.; Hasegawa, T.; Nakayama, T.; Aono, M. Quantized Conductance Atomic Switch. *Nature* **2005**, *433*, 47−50.
(24) Waser, R.; Aono, M. Nanoionics-Based Resistive Switching Memories. *Nat. Mater.* **2007**, *6*, 833−840.
(25) Esteban, R.; Borisov, A. G.; Nordlander, P.; Aizpurua, J. Bridging Quantum and Classical Plasmonics with a Quantum-Corrected Model. *Nat. Commun.* **2012**, *3*, 825.
(26) Pérez-González, O.; Zabala, N.; Borisov, A. G.; Halas, N. J.; Nordlander, P.; Aizpurua, J. Optical Spectroscopy of Conductive Junctions in Plasmonic Cavities. *Nano Lett.* **2010**, *10*, 3090−3095.
(27) Scholl, J. A.; García-Etxarri, A.; Koh, A. L.; Dionne, J. A. Observation of Quantum Tunneling between Two Plasmonic Nanoparticles. *Nano Lett.* **2013**, *13*, 564−569.
(28) Schnell, M.; Garcia Etxarri, A.; Huber, A. J.; Crozier, K.; Aizpurua, J.; Hillenbrand, R. Controlling the Near-Field Oscillations of Loaded Plasmonic Nanoantennas. *Nat. Photonics* **2009**, *3*, 287−291.
(29) Chua, L. Resistance Switching Memories Are Memristors. *Appl. Phys. A: Mater. Sci. Process.* **2011**, *102*, 765−783.
(30) Weber, D.; Katzmann, J.; Neubrech, F.; Härtling, T.; Pucci, A. Spectral Tuning of IR-Resonant Nanoantennas by Nanogap Engineering. *Opt. Mater. Express* **2011**, *1*, 1301−1306.
(31) Wang, G.; Chen, X.; Liu, S.; Wong, C.; Chu, S. Mechanical Chameleon through Dynamic Real-Time Plasmonic Tuning. *ACS Nano* **2016**, *10*, 1788−1794.
(32) Emboras, A.; Goykhman, I.; Desiatov, B.; Mazurski, N.; Stern, L.; Shappir, J.; Levy, U. Nanoscale Plasmonic Memristor with Optical Readout Functionality. *Nano Lett.* **2013**, *13*, 6151−6155.
(33) Emboras, A.; Niegemann, J.; Ma, P.; Haffner, C.; Pedersen, A.; Luisier, M.; Hafner, C.; Schimmel, T.; Leuthold, J. Atomic Scale Plasmonic Switch. *Nano Lett.* **2016**, *16*, 709−714.
(34) Wong, H. S. P.; Lee, H. Y.; Yu, S.; Chen, Y. S.; Wu, Y.; Chen, P. S.; Lee, B.; Chen, F. T.; Tsai, M. J. Metal Oxide RRAM. *Proc. IEEE* **2012**, *100*, 1951−1970.
(35) Chen, J.-Y.; Hsin, C.-L.; Huang, C.-W.; Chiu, C.-H.; Huang, Y.-T.; Lin, S.-J.; Wu, W.-W.; Chen, L.-J. Dynamic Evolution of Conducting Nanofilament in Resistive Switching Memories. *Nano Lett.* **2013**, *13*, 3671−3677.
(36) Gopalan, C.; Ma, Y.; Gallo, T.; Wang, J.; Runnion, E.; Saenz, J.; Koushan, F.; Hollmer, S. Demonstration of Conductive Bridging Random Access Memory (CBRAM) in Logic CMOS Process. *IEEE International Memory Workshop* **2010**, 1−4.
(37) Inan, U. S.; Marshall, R. A. *Numerical Electromagnetics: The FDTD Method*; Cambridge University Press: Cambridge, 2011.
(38) Larentis, S.; Nardi, F.; Balatti, S.; Gilmer, D. C.; Ielmini, D. Resistive Switching by Voltage-Driven Ion Migration in Bipolar RRAM—Part II: Modeling. *IEEE Trans. Electron Devices* **2012**, *59*, 2468−2475.
(39) Qin, S.; Liu, Z.; Zhang, G.; Zhang, J.; Sun, Y.; Wu, H.; Qian, H.; Yu, Z. Atomistic Study of Dynamics for Metallic Filament Growth in Conductive-Bridge Random Access Memory. *Phys. Chem. Chem. Phys.* **2015**, *17*, 8627−8632.
(40) Alù, A.; Engheta, N. Input Impedance, Nanocircuit Loading, and Radiation Tuning of Optical Nanoantennas. *Phys. Rev. Lett.* **2008**, *101*, 043901.
(41) Alu, A.; Engheta, N. Tuning the Scattering Response of Optical Nanoantennas with Nanocircuit Loads. *Nat. Photonics* **2008**, *2*, 307−310.
(42) Engheta, N.; Salandrino, A.; Alù, A. Circuit Elements at Optical Frequencies: Nanoinductors, Nanocapacitors, and Nanoresistors. *Phys. Rev. Lett.* **2005**, *95*, 095504.
(43) Shi, J.; Monticone, F.; Elias, S.; Wu, Y.; Ratchford, D.; Li, X.; Alù, A. Modular Assembly of Optical Nanocircuits. *Nat. Commun.* **2014**, DOI: 10.1038/ncomms4896.
(44) Liu, N.; Wen, F.; Zhao, Y.; Wang, Y.; Nordlander, P.; Halas, N. J.; Alù, A. Individual Nanoantennas Loaded with Three-Dimensional Optical Nanocircuits. *Nano Lett.* **2013**, *13*, 142−147.
(45) Romano, J. D.; Price, R. H. The Conical Resistor Conundrum: A Potential Solution. *Am. J. Phys.* **1996**, *64*, 1150−1153.
(46) Chan, G. H.; Zhao, J.; Hicks, E. M.; Schatz, G. C.; Van Duyne, R. P. Plasmonic Properties of Copper Nanoparticles Fabricated by Nanosphere Lithography. *Nano Lett.* **2007**, *7*, 1947−1952.
(47) Ordal, M. A.; Long, L. L.; Bell, R. J.; Bell, S. E.; Bell, R. R.; Alexander, R. W.; Ward, C. A. Optical Properties of the Metals Al, Co, Cu, Au, Fe, Pb, Ni, Pd, Pt, Ag, Ti, and W in the Infrared and Far Infrared. *Appl. Opt.* **1983**, *22*, 1099−1119.
(48) Palik, E. D.; Ghosh, G. *Handbook of Optical Constants of Solids*; Academic Press: San Diego, 1998.
(49) Yi, J.; Kim, S.-W.; Nishi, Y.; Hwang, Y.-T.; Chung, S.-W.; Hong, S.-J.; Park, S.-W. Research on Switching Property of an Oxide/Copper Sulfide Hybrid Memory. In *Non-Volatile Memory Technology Symposium*; IEEE: Pacific Grove, CA, 2008; pp 1−4. 10.1109/NVMT.2008.4731189
(50) Kim, S.-W.; Nishi, Y. Copper Sulfide-Based Resistance Change Memory in *2007 Non-Volatile Memory Technology Symposium*; IEEE: Albuquerque, **2007**; pp 76−78. 10.1109/NVMT.2007.4389951
(51) Prangsma, J. C.; Kern, J.; Knapp, A. G.; Grossmann, S.; Emmerling, M.; Kamp, M.; Hecht, B. Electrically Connected Resonant Optical Antennas. *Nano Lett.* **2012**, *12*, 3915−3919.
(52) Jo, G.; Choe, M.; Lee, S.; Park, W.; Kahng, Y. H.; Lee, T. The Application of Graphene as Electrodes in Electrical and Optical Devices. *Nanotechnology* **2012**, *23*, 112001.
(53) Minami, T. Transparent Conducting Oxide Semiconductors For Transparent Electrodes. *Semicond. Sci. Technol.* **2005**, *20*, S35.
(54) Saadeldin, M.; Soliman, H. S.; Ali, H. A. M.; Sawaby, K. Optical and Electrical Characterizations of Nanoparticle Cu2S Thin Films. *Chin. Phys. B* **2014**, *23*, 046803.
(55) Pan, F.; Subramanian, V. A Kinetic Monte Carlo Study on the Dynamic Switching Properties of Electrochemical Metallization RRAMs During the SET Process. *International Conference on Simulation of Semiconductor Processes and Devices* **2010**, 19−22.
(56) Yu, N.; Genevet, P.; Kats, M. A.; Aieta, F.; Tetienne, J.-P.; Capasso, F.; Gaburro, Z. Light Propagation with Phase Discontinuities: Generalized Laws of Reflection and Refraction. *Science* **2011**, *334*, 333−337.
(57) Wu, C.; Arju, N.; Kelp, G.; Fan, J. A.; Dominguez, J.; Gonzales, E.; Tutuc, E.; Brener, I.; Shvets, G. Spectrally Selective Chiral Silicon Metasurfaces Based on Infrared Fano Resonances. *Nat. Commun.* **2014**, *5*,.10.1038/ncomms4892
(58) Wu, C.; Khanikaev, A. B.; Adato, R.; Arju, N.; Yanik, A. A.; Altug, H.; Shvets, G. Fano-Resonant Asymmetric Metamaterials for Ultrasensitive Spectroscopy and Identification of Molecular Monolayers. *Nat. Mater.* **2011**, *11*, 69−75.
(59) Zhang, S.; Genov, D. A.; Wang, Y.; Liu, M.; Zhang, X. Plasmon-Induced Transparency in Metamaterials. *Phys. Rev. Lett.* **2008**, *101*, 047401.
(60) Sun, P.; Li, L.; Lu, N.; Li, Y.; Wang, M.; Xie, H.; Liu, S.; Liu, M. Physical Model of Dynamic Joule Heating Effect for Reset Process in Conductive-Bridge Random Access Memory. *J. Comput. Electron.* **2014**, *13*, 432−438.
(61) Fowler, R. H.; Nordheim, L. Electron Emission in Intense Electric Fields. *Proc. R. Soc. London, Ser. A* **1928**, *119*, 173−181.



DOI: 10.1021/acsnano.6b02031
*ACS Nano* 2016, 10, 6716−6724